Preparation of high-performance multiphase heterostructures IT-SOFC cathode materials by Pr-induced in situ assembly

Jinghe Bai [a], Defeng Zhou [a,*], Leilei Niu [a], Xiaofei Zhu [a,*], Ning Wang [b,*], Qingwen Liang [b], Youjie Zhang [a], Ling Hu [a], Huifang Gong [a], Wenfu Yan [c]

[a] School of Chemistry and Life Science, Changchun University of Technology, Changchun 130012, China
[b] Shenzhen Institute of Advanced Electronic Materials, Shenzhen Institute of Advanced Technology, Chinese Academy of Sciences, Shenzhen 518055, China
[c] State Key Laboratory of Inorganic Synthesis and Preparative Chemistry, College of Chemistry, Jilin University, Changchun 130012, China

ARTICLE INFO

ABSTRACT

Here, in situ assembly in $La_{0.6}Sr_{0.4}Co_{0.2}Fe_{0.8}O_{3-\delta}$ and $CoFe_2O_4$ composite (LSCFC) cathode was induced by Pr to form $La_{0.6}Sr_{0.4}Co_xFe_yO_{3-\delta}/PrCoO_3/Co_3O_4/PrO_2$ (LSCFC-PI) multiphase heterostructures. The surface of LSCFC-PI forms uniform nanoparticles, and the unique core-shell structure prevents Sr segregation, thereby enhancing CO_2 tolerance and increasing oxygen reduction reaction (ORR) active sites. Furthermore, compared with LSCFC, LSCFC-PI increases the oxygen vacancy content of the cathode due to the existence of multiphase heterostructure, improves the ORR kinetics, and the conductivity is also greatly improved. The peak power density (PPD) of LSCFC-PI as a single-cell cathode at 700 °C reached 1.51 W cm^{-2}, which was 2.65 times higher than that of LSCFC's 0.57 W cm^{-2}, and in the long-term stability test at a constant voltage ~0.8 V for 100 hours, showing excellent stability. In situ assembly of multiphase heterostructures is expected to become a new strategy for developing high-performance IT-SOFC cathodes.

1. Introduction

With the rapid advancement of the global industrialization, the continuous consumption of traditional fossil fuels and non-renewable energy sources and the excessive emission of CO_2 have led to the continuous aggravation of the greenhouse effect [1]. In recent years, the research and development of clean energy has become a research hotspot. Solid oxide fuel cell (SOFC) as an energy conversion device that can efficiently convert the chemical energy inside a variety of fuels into electrical energy [2]. However, the high operating temperature (800–1000℃) of SOFC seriously damages the compatibility between components and connection materials, resulting in the degradation of cell performance and limiting its commercialization [3,4]. Therefore, lowering the temperature to an intermediate-temperature (IT: 600–800 ℃) environment is a key factor for the commercialization of SOFC.

Currently, the slow kinetics of the oxygen reduction reaction (ORR) at the cathode in an intermediate-temperature environment and the rapid ORR decay in a CO_2 environment limit the electrocatalytic activity and stability of SOFC. Therefore, we need to improve the ORR activity and stability of cathode materials to enhance the application prospects

of IT-SOFC [5,6]. Wang et al. [7]. attached a layer of PrO_2 with high ORR activity on the surface of $(La_{0.6}Sr_{0.4})_{0.95}Co_{0.2}Fe_{0.8}O_{3-\delta}$ (LSCF) by impregnation method, thereby forming a heterointerfaces between LSCF and PrO_2, which effectively enhanced the cathode surface's ORR kinetics; At 600 ℃, the ASR value of LSCF/PrO_2 reaches 0.241 Ω cm^2, representing only 33% of that of pristine LSCF. Although the impregnation technique can enhance the ORR activity on the cathode surface, the impregnation liquid is mainly concentrated in the upper layer, so the uniformity between the two phases is difficult to control, and thus the surface deposition phenomenon is more prone to occur. To better control the uniform distribution of the heterointerface, in situ assembly is currently one of the most effective methods. Chen et al. [8]. promoted the ORR dynamics of the cathode by partially decomposing the $PrBa_{0.8}Ca_{0.2}Co_2O_{5+\delta}$ phase during the preparation of the 40 wt% $Gd_{0.2}Ce_{0.8}O_{1.9}$-$PrBa_{0.8}Ca_{0.2}Co_2O_{5+\delta}$ (40GDC-PBCC) cathode and forming a heterostructure with $PrBa_{0.8}Ca_{0.2}Co_2O_{5+\delta}/Gd_{0.2}Ce_{0.8}O_{1.9}/BaCoO_{3-\delta}$ by in situ assembly. Furthermore, uniform nanoparticles are formed on the surface of the in situ assembled cathode, and the unique core-shell structure can not only increase the number of ORR active sites of the cathode but also improve the adhesion of the cathode

---

* Corresponding authors.
  E-mail addresses: defengzhou65@126.com (D. Zhou), zhuxiaofei@ccut.edu.cn (X. Zhu), wangning@siat.ac.cn (N. Wang).

to the electrolyte [9,10]. The single cell prepared with 40GDC-PBCC cathode achieved a PPD of 1.74 W cm^{-2} at 750 ℃ and exhibited excellent long-term stability during 200 h of operation. Lu et al. [11]. formed a simple perovskite structure on the surface of the double perovskite by using in situ exsolution technology on PrBa$_{0.94}$Co$_2$O$_{5+\delta}$ with A-site defects, and the heterointerface formed between the two phases promoted the ORR kinetics of the cathode. The ASR of the cathode reaches 0.025 Ω cm^2 at 700 ℃. Geng et al. [12]. soaked SrFe$_{0.9}$Nb$_{0.1}$O$_{3-\delta}$ in Sr(NO$_3$)$_2$ solution and then calcined for 1050 ℃ to prepare SrFe$_{0.9}$Nb$_{0.1}$O$_{3-\delta}$@Sr$_3$Fe$_{1.8}$Nb$_{0.2}$O$_{7-\delta}$ with a core-shell structure. The heterointerface between the two phases improved the oxygen exchange capacity of the cathode surface; The PPD of the single cell prepared with SrFe$_{0.9}$Nb$_{0.1}$O$_{3-\delta}$@Sr$_3$Fe$_{1.8}$Nb$_{0.2}$O$_{7-\delta}$ as the cathode reaches 0.347 W cm^{-2} at 700 ℃, which is approximately 1.53 times higher than that of the pristine SrFe$_{0.9}$Nb$_{0.1}$O$_{3-\delta}$ (0.227 W cm^{-2}). Zhou et al. [13]. used the A-site non-stoichiometry to increase the content of Pr when preparing Pr$_{0.5}$Sr$_{0.5}$MnO$_{3-\delta}$, and induced Pr to exsolution to the surface to form a cathode with Pr$_{0.5}$Sr$_{0.5}$MnO$_{3-\delta}$/PrO$_2$ structure; Experiments combined with first-principles calculations confirmed that the construction of the heterointerface can help reduce the oxygen vacancy formation energy to accelerate the ORR kinetics of the cathode, and has excellent CO$_2$/H$_2$O tolerance.

In summary, a uniform heterostructure can not only promote the ORR kinetics inside the cathode but also effectively increase the ORR active sites on the cathode surface. Previous related studies have shown that although PrO$_2$ is not a suitable material for SOFC cathode materials, the cathode surface modified by PrO$_2$ has excellent ORR activity due to its low oxygen vacancy formation energy [14]. In addition, previous research has mainly focused on constructing heterointerface between two phases. In this study, La$_{0.6}$Sr$_{0.4}$Co$_{0.2}$Fe$_{0.8}$O$_{3-\delta}$ and CoFe$_2$O$_4$ composite (LSCFC) cathodes were prepared by configuring a stoichiometric ratio below the tolerance factor (<0.75) range of perovskite. The LSCFC cathode was soaked in Pr(NO$_3$)$_3$ solution, and after calcination, the internal second phase CoFe$_2$O$_4$ decomposes. Pr induces in situ assembly of LSCFC to form a multiphase heterointerface with La$_{0.6}$Sr$_{0.4}$Co$_x$Fe$_y$O$_{3-\delta}$/PrCoO$_3$/Co$_3$O$_4$/-PrO$_2$ structure. Through systematic experiments, it has been shown that in situ assembly of multiphase heterostructures can not only improve the ORR activity of the cathode, but also exhibit excellent CO$_2$ tolerance due to its unique core-shell structure.

2. Experiment

2.1. Material preparation

Weigh La(NO$_3$)$_2$·6 H$_2$O (99.9%, aladdin), Sr(CH3COO)$_2$ (99.9%, aladdin), Co(NO$_3$)$_2$·6 H$_2$O (99.9%, aladdin), and Fe(NO$_3$)$_3$·9 H$_2$O (99.9%, aladdin) according to the Chemical Structure of (La$_{0.6}$Sr$_{0.4}$)$_{0.7}$-Co$_{0.2}$Fe$_{0.8}$O$_{3-\delta}$ (LSCFC), then add citric acid (2 g, 99.5%, Beijing Chemical Industry) and polyethylene glycol (1 g, aladdin), and stir well in deionized water until the solution is completely dissolved. The prepared precursor solution was transferred to a water bath at 80 ℃ for heating and volatilization to form a xerogel and then heated by an electric furnace until it spontaneously ignited to form a black powder. The powder was pre-calcined at 600 ℃ for 5 hours (h), then fully ground, and finally calcined at 950 ℃ for 2 h to obtain LSCFC. The prepared LSCFC was dissolved in three different concentrations of Pr(NO$_3$)$_2$ solution for 8 h, and then ultrasonic for 30 min after drying at 80 ℃ and fully grinding to prepare the required cathode powder. The concentration ratio of Pr(NO$_3$)$_2$ solution is in Table S1. For the convenience of distinction and discussion, we labeled the cathodes prepared with low, intermediate, and high concentrations of Pr(NO$_3$)$_2$ as LSCFC-PL, LSCFC-PI, and LSCFC-PH, respectively. The preparation of Gd$_{0.2}$Ce$_{0.8}$O$_{2-\delta}$ (GDC) electrolyte can refer to our previous research [15,16]. Conductivity sample strips were obtained by pressing the powder into strips (28 mm × 0.4 mm × 0.5 mm) under a pressure of 15 MPa, followed by calcination at 900 ℃ for 10 h.

2.2. Preparation of cell

Symmetrical cell: The ethyl cellulose and terpineol (94 wt%: 6 wt%) were prepared as a binder, and the slurry was prepared by combining the binder with the cathode, which was subsequently screen-printed on both sides of the GDC. The cathode's effective active area measures 0.2 cm^2, and it was calcined at 900 ℃ for 2 h. Single cell: The prepared cathode slurry was screen-printed onto a commercial half-cell NiO-YSZ| YSZ|GDC(Ningbo SOFCMAN Energy Co. Ltd.), the effective area of the electrode was consistent with that of a symmetrical cell, and then calcined at 900 ℃ for 2 h. The fuel cell was affixed to one end of the corundum tube and hermetically sealed on the anode side using conductive silver paste (DAD-87).

2.3. Characterization

Using an X-ray diffractometer (Bruker/Advance X, USA) and a Cu Kα X-ray source (λ = 0.15406 nm, 40 kV, and 10 mA) at room temperature, the scan rate was 3 min per degree, and the step size was 0.02°. The scanning range is 20–80°. XRD data was Rietveld refined using FullProf software. The prepared samples were subjected to a thermogravimetric analysis (NETZSCH, STA-449F3) test under N$_2$ environment using a thermogravimetric analyzer, and data were collected at 30–800 ℃ with a heating rate of 10 ℃ min^{-1}. The morphology of the material was analyzed by field emission scanning electron microscopy (FE-SEM, JEOL7610), and the distribution and content of elements were characterized using elemental mapping and energy dispersive spectroscopy. The spatial arrangement structure and element distribution of the crystals were analyzed by a high-resolution transmission electron microscope (HR-TEM, JEOL JEM-2100-F, Japan) with an accelerating voltage of 200 kV. The chemical states of the sample surface elements were analyzed by X-ray photoelectron spectroscopy (XPS, VG ESCALAB 250). The electrochemical workstation (1260/1287, Solartron) is in the frequency range of 10^{-1}-10^6 Hz, with an interference signal of 10 mV, to perform electrochemical impedance spectroscopy (EIS) tests and single-cell I-V curve tests. Calculate the activation energy between ASR and temperature (*T*) based on the following formula [17]:

$$\frac{1}{ASR} = A\exp\left(-\frac{E_a}{RT}\right) \tag{1}$$

Among them, *R* and *A* are the universal gas constant (8.314 J mol^{-1} K^{-1}) and pre-exponential factors, respectively. The electrical conductivity was calculated by EIS testing a dense cathode sample strip in the range of 100–800 ℃ by the following formula:

$$\sigma = \frac{L}{RS} \tag{2}$$

Where σ is the conductivity, R, S, and L are the resistance, cross-sectional area, and length of the sample strip. The electrical conductivity relaxation (ERC) curve is obtained by testing the electrical conductivity sample strip under the condition of converting the mixed gas (air and N$_2$ are mixed at flow rates of 50 mL min^{-1} and 50 mL min^{-1}, respectively) to air (100 mL min^{-1}), and fitting the ECR curve using the formula in the supporting material to obtain the chemical bulk diffusion coefficient (D$_{chem}$) and surface exchange coefficient (k$_{chem}$) of the cathode. In a vacuum environment, the N$_2$ adsorption-desorption isothermal test (ASAP 2010, Micromeritics) was carried out at a constant temperature of 180 ℃ for 10 h, and the specific surface area was measured in combination with the Bruner-Emitter-Teller (BET) isothermal technique. The oxygen vacancies of the samples were tested by electron paramagnetic resonance (EPR, Bruker A300) at room temperature and air environment. The functional groups of the samples after CO$_2$ heat treatment were tested using Fourier transform infrared (FT-IR) spectroscopy.

3. Results and discussion

3.1. Phase structure and micromorphology

To observe the internal structure of the as-prepared cathodes, we performed XRD tests on all the samples. Fig. 1(a) shows the XRD patterns of LSCFC and LSCFC-PI and the corresponding crystal structure standard peaks; Fig. 1(b) shows the XRD pattern of all cathodes. It can be seen that LSCFC is not a pure perovskite structure, and there are characteristic peaks of $CoFe_2O_4$ spinel structure. This is primarily attributed to the low content of A-site cations. To maintain the stability of the perovskite structure as much as possible, the segregation of B-site cations forms $CoFe_2O_4$ with a spinel structure [18–20]. In addition, a small number of characteristic peaks of cubic fluorite structure appeared in the internal structure of the sample after adding $Pr(NO_3)_3$ modification and calcination, which is because Pr ions reacted with oxygen to form PrO_2 during high-temperature calcination [7]. Fig. 1(c-d) and Figure S1 shows the Rietveld refined XRD patterns of LSCFC, LSCFC-PI, LSCFC-PL, and LSCFC-PH, respectively. The Pm-3 m, Fd-3 m, and Fm-3 m spatial groups belong to the perovskite, spinel, and cubic fluorite structures, respectively. It can be seen that there are two types of crystals inside LSCFC: perovskite and spinel. However, after adding Pr ions, a small amount of cubic fluorite structure appeared inside the cathode, and the weight percentage of perovskite and spinel changed, indicating that Pr ions can alter the internal structural composition of LSCFC.

To understand the difference in morphology between different cathodes, we observed the morphology of all cathodes by FE-SEM. It can

be seen from Fig. 2(a) that the grain size of LSCFC is larger and the surface is smoother. However, the surface of the modified LSCFC-PL in Fig. 2(b) begins to form nanoscale particles, and the core-shell structure prepared by in situ assembly is beneficial for increasing the specific surface area of the cathode. Fig. 2(c-d) shows that the surface roughness of LSCFC-PI further increases, and LSCF-PH exhibits agglomeration. In addition, the specific surface area of LSCFC and LSCFC-PI is also compared in Figure S2. The specific surface area of LSCFC is only 3.34 m^2 g^{-1}, while that of LSCFC-PI is 12.16 m^2 g^{-1}, which is mainly because the contact area with oxygen is fully improved by the nanoparticles formed on the surface [7].

To understand the effect of the addition of Pr ions on the internal structure of LSCFC, Fig. 3(a-b) shows the TEM and HR-TEM images of LSCFC-PI, where the inset in Fig. 3(b) is the inverse fast Fourier transform (IFFT) in the corresponding region Image. Two different crystal structures can be seen in Fig. 3(b), and there is an obvious heterointerface between the two phases. Fig. 3(c-d) shows a fast Fourier transform diagram (FFT) in the yellow and red regions in Fig. 3(b). According to FFT images, there is perovskite with a Pm-3 m space group and spinel with an Fd-3 m space group in LSCFC-PI. Among them, the lattice spacing belonging to perovskite is $d_{(100)}$=0.388 nm [21], and the lattice spacing belonging to spinel is $d_{(220)}$=0.292 nm [22]. Fig. 3(e) shows the corresponding line intensity distribution, which further verifies the accuracy of the lattice spacing; Fig. 3(f-g) shows the elemental mapping images of LSCFC-PI and LSCFC, respectively. It can be seen that all elements of LSCFC are evenly distributed without obvious agglomeration, but the Co element of LSCFC-PI forms nanoparticles on the
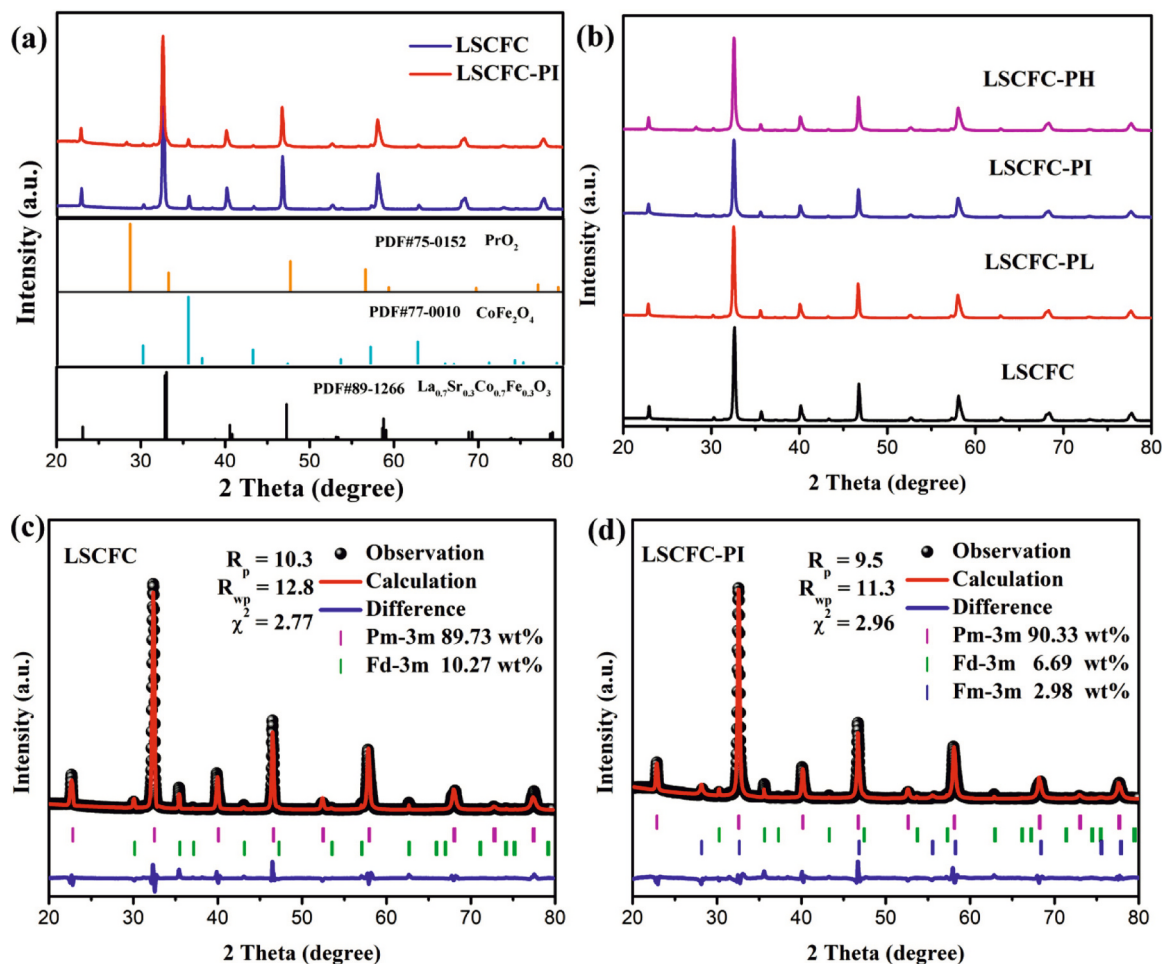

Fig. 1. (a) XRD patterns of LSCFC, LSCFC-PI, and corresponding crystal structures, (b) XRD patterns of all cathodes, (c-d) Rietveld refined patterns of XRD of LSCFC and LSCFC-PI.
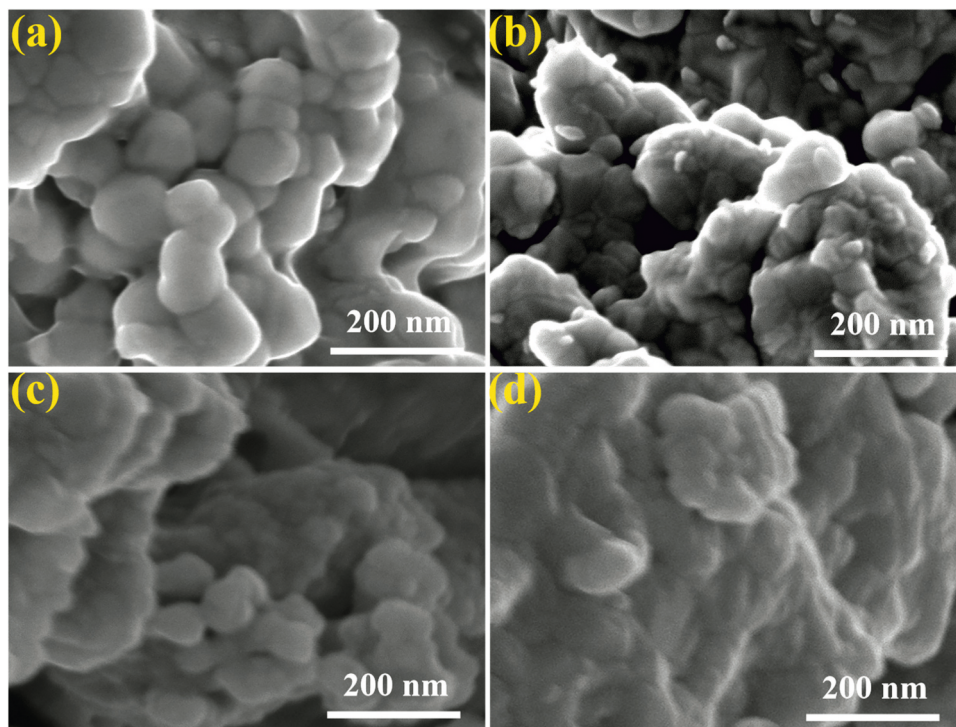
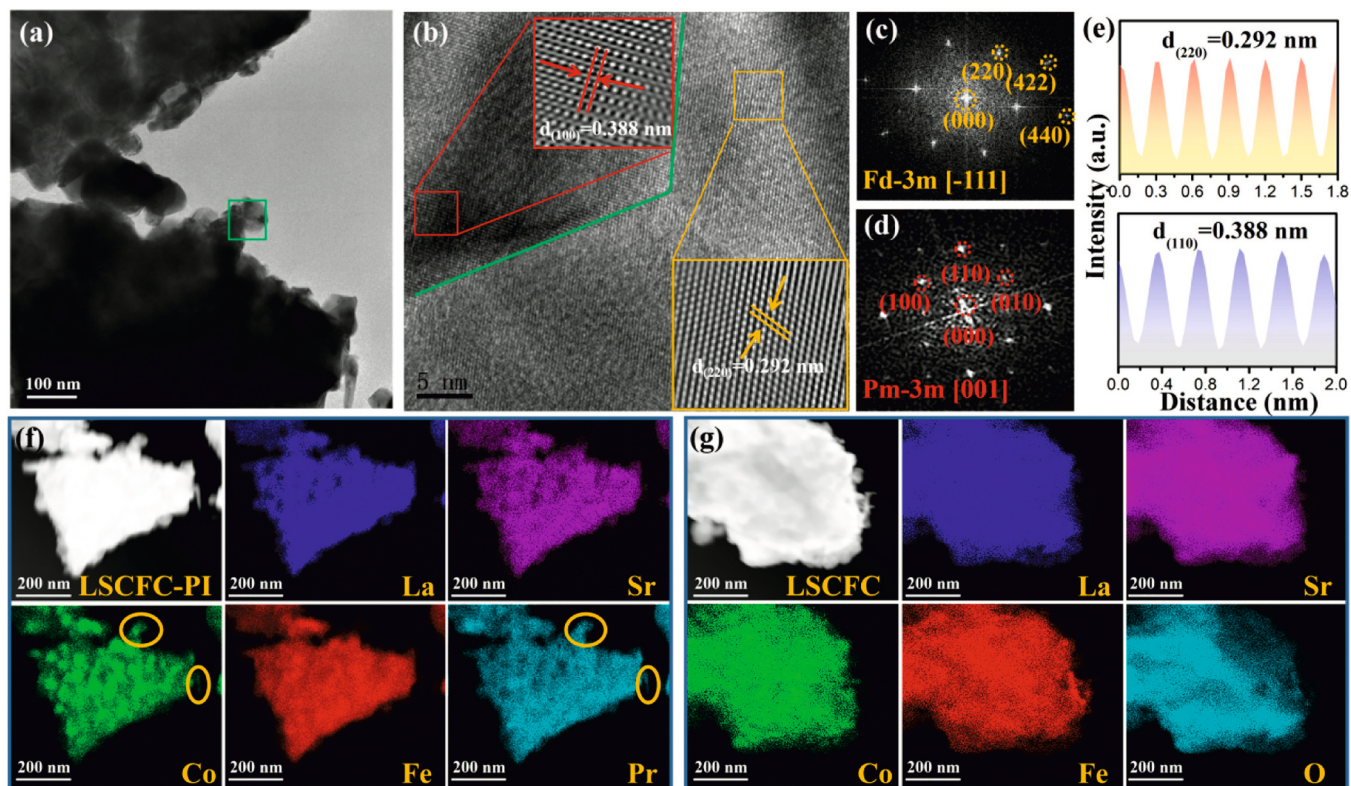**Fig. 2.** (a-d) FE-SEM images of LSCFC, LSCFC-PL, LSCFC-PI, LSCFC-PH.

Fig. 3. (a) TEM image of LSCFC-PI and (b) HR-TEM image (the inset is the corresponding IFFT image), (c-d) corresponds to the FFT image in the yellow and red regions in (b) and (e) the corresponding line intensity distributed; (f) elemental mapping image of LSCFC-PI, (g) elemental mapping image of LSCFC.

surface. Based on the analysis in Fig. 3(b), it can be concluded that the Pr ion in LSCFC-PI induces in situ self-assembly of the cathode surface to form Co_3O_4 and $PrCoO_3$ nanoparticles. In addition, according to the mapping image of LSCFC-PI in Figure S3, the phase of PrO_2 was also

captured. A large number of previous studies have shown that PrO_2 attached to the cathode surface has low oxygen vacancy formation energy, which can effectively improve the ORR activity at the interface [7, 14,21,23]. The formation of this multiphase structure is mainly due to

the poor structural stability when the A-site stoichiometry of the pre-pared LSCF reaches 0.7, resulting in the recombination of recombination of segregated B-site cations and Pr ions. Figure S4 and Figure S5 discuss in detail the structural differences between LSCF and Pr composites with different stoichiometric numbers at A-site, and the reasons for the formation of uniform multiphase heterostructures in LSCFC-PI. The above results indicate that the nanoparticles on the surface of LSCFC-PI are a core-shell nanostructure formed by multiphase uniform mixing with intertwining. Therefore, we found that LSCFC-PI is a cathode assembled in situ with a $La_{0.6}Sr_{0.4}Co_xFe_yO_{3-\delta}/PrCoO_3/Co_3O_4/PrO_2$-type hetero-structure. Generally, the formation of heterostructures contributes to the ORR kinetics of cathodes [14,24–27].

3.2. Surface chemical environment of the elements in the sample

The surface chemical environments of different samples were dis-cussed and analyzed in detail using XPS. Fig. 4(a) shows the full XPS spectra of all cathodes, and the characteristic peaks corresponding to all elements have been detected. Fig. 4(b) shows the O 1 s XPS spectra of all cathodes, in which lattice oxygen O_{lat} has the lowest binding energy (~527.5 eV), the intermediate binding energy (~529.8 eV) adsorbs oxygen O_{ads} on the cathode surface, and the oxygen in water molecules has the highest binding energy (~532.1 eV). The surface O_{ads} are frequently linked to the oxygen vacancy content within the cathode [28, 29]. By comparing the O 1 s of all cathodes, the order of the surface O_{ads}

content is obtained: LSCFC (40.3%) < LSCFC-PL (41.9%) < LSCFC-PH (43.8%) < LSCFC-PI (44.8%); It can be found that the addition of Pr can increase the cathode O_{ads} content and the O_{ads} of LSCFC-PI is the highest. In addition, Fig. 4(c) shows an XPS spectra of Sr 3d orbitals in all cathodes. Usually, the existing form of Sr element is similar to that of O, and there are lattice Sr (Sr_{lat}) and surface Sr ($Sr_{surface}$). Due to the high oxidation and low electronegativity of Sr element, it is easy to react with O_2, H_2O, and CO_2 gases in the external environment to generate SrO, Sr $(OH)_2$, $SrCO_3$ insulating phases covering the cathode surface, which reduces the number of ORR sites in the cathode. Therefore, the higher the $Sr_{surface}$ content, it is detrimental to both the ORR activity and sta-bility of the cathode [30,31]. It can be seen from the comparison that the higher the Sr_{lat} of the cathode with the increase of the Pr content, the more stable the structure of the cathode; This is mainly because in the cathode, the nanoparticles formed by Pr-induced in situ assembly on the cathode surface hinder the path of Sr towards surface segregation [10]; In addition, the Pr ions increases the acidity of the cathode and hinders the generation of alkaline substances, thus reducing the content of $Sr_{surface}$ [32,33]. Through Table 1, the percentages of O_{lat}, O_{ads}, Sr_{lat}, and $Sr_{surface}$ in the cathode can be observed more intuitively.

In addition, we also observed the valence changes of all cathode B-site ions, and Fig. 4(d–e) shows the XPS spectra of the 2p orbitals of Co and Fe, respectively. Generally, Fe ions exist in a state of mixed valence encompassing $Fe^{2+}/Fe^{3+}/Fe^{4+}$ [34–36], in which Fe^{2+} exhibits the lowest binding energy ($2p_{3/2}$: ~709.2 eV; $2p_{1/2}$: ~722.4 eV), Fe^{3+} has
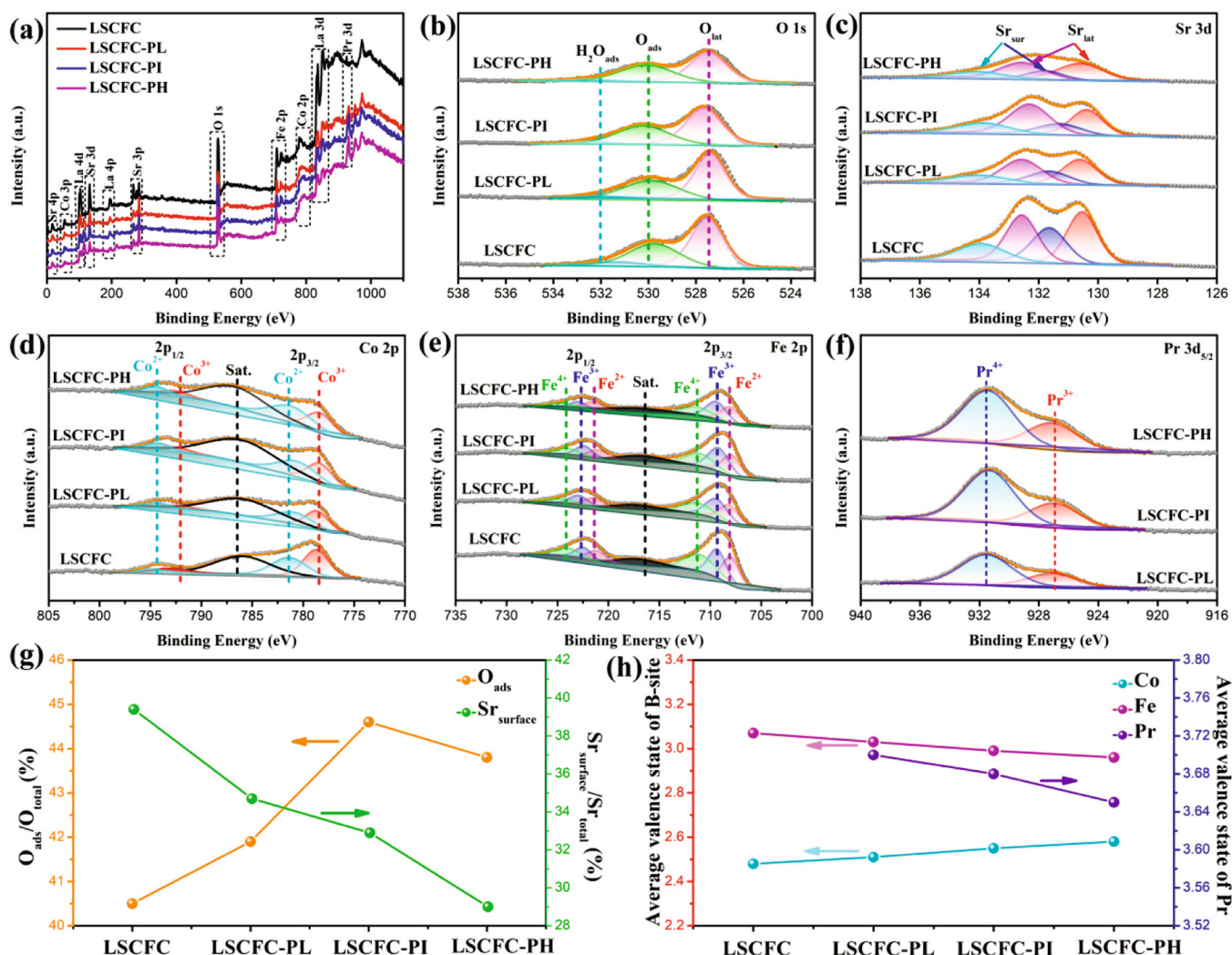

Fig. 4. (a) Full XPS spectra of all samples and XPS spectra of (b) O 1 s, (c) Sr 3d, (d) Co 2p, (e) Fe 2p, (f) Pr $3d_{5/2}$.

Table 1
Percentage of O_{lat}, O_{ads}, Sr_{lat}, and $Sr_{surface}$ in all cathodes.

Cathode	O_{lat} (%)	O_{ads} (%)	Sr_{lat} (%)	Sr_{sur} (%)
LSCFC	59.7	40.3	60.6	39.4
LSCFC-PL	58.1	41.9	65.3	34.7
LSCFC-PI	55.2	44.8	67.2	32.8
LSCFC-PH	56.2	43.8	71.0	29.0

the middle binding energy ($2p_{3/2}$: ~709.2 eV; $2p_{1/2}$: ~722.4 eV), and Fe^{4+} possesses the highest binding energy ($2p_{3/2}$: ~711.0 eV; $2p_{1/2}$: ~724.1 eV). Co ions exist in the form of Co^{2+}/Co^{3+} [24,37,38], with Co^{2+} having the highest binding energy ($2p_{3/2}$: ~780.6 eV; $2p_{1/2}$: ~794.1 eV) and Co^{3+} having the lowest binding energy($2p_{3/2}$: ~778.3 eV; $2p_{1/2}$: ~792.6 eV). By comparison, it was found that with the increase of Pr ions, the valence of Fe ions showed a downward trend, while the valence of Co ions showed an upward change. This is because LSCFC is a mixture of $La_{0.6}Sr_{0.4}Co_{0.2}Fe_{0.8}O_{3-\delta}$ (LSCF) and $CoFe_2O_4$ crystals, and the material structure of the spinel structure is relatively stable without internal oxygen vacancies, so the valences of Co and Fe in $CoFe_2O_4$ are +2 and +3. From the change of O_{ads} content, it can be seen that Pr ions can induce oxygen vacancies in LSCFC. It can be attributed to the redox reaction of B-site ions in LSCFC, and the valence of Co ions showed an upward trend. Combined with the nanoparticles on the cathode surface in Fig. 3, it is further confirmed that the addition of Pr ions decomposes $CoFe_2O_4$ and induces the oxidation of $Co^{2+}$to Co^{3+}, replacing the Fe^{3+} in $CoFe_2O_4$ to form Co_3O_4, and another part combines with Pr^{3+} ions to form $PrCoO_3$; In addition, Fe^{3+} (0.645 Å) with smaller radius is reduced to Fe^{2+} (0.780 Å) with larger radius into LSCF to replace Co^{2+} (0.745 Å), which improves the fitness of A-site and B-site ions in the perovskite structure and thus improves the structural stability of perovskite (La^{3+} radius = 1.032 Å, Sr^{2+} radius = 1.180 Å). Usually, the occurrence of oxygen vacancies in the cathode is accompanied by the reduction reaction of B-site ions [39]. The reaction equation is as follows:

$$2Fe_{Fe}^{\bullet} + O_O^X \Leftrightarrow 2Fe_{Fe}^X + V_O^{\bullet\bullet} + \frac{1}{2}O_2 \qquad (3)$$

$$2Fe_{Co}^{\bullet} + O_O^X \Leftrightarrow 2Fe_{Fe}^X + V_O^{\bullet\bullet} + \frac{1}{2}O_2 \qquad (4)$$

Among them, Fe_{Fe}^X, $Fe_{Fe}^{\bullet}$, and $Fe_{Co}^{\bullet}$ represent $Fe^{2+}(Fe^{3+})$, $Fe^{3+}(Fe^{4+})$, and Co^{2+} occupying the Fe^{3+} position, respectively. Fig. 4(f) corresponds to the XPS spectra of the Pr $3d_{5/2}$ orbitals of different cathodes, in which as the content of Pr ions increases, the proportion of Pr^{3+} ions is also higher, which further confirms the generation of $PrCoO_3$. Fig. 4(g) shows the curve that changes the percentage of O_{ads} and $Sr_{surface}$ with the content of Pr ion. Fig. 4(h) shows the curve of the average valency of Co, Fe, and Pr as the content of Pr ion changes. Table 2 is a summary of the average valences of Co, Fe, and Pr ions in cathodes. It can be seen from Fig. 4(g-h) that all elements except O_{ads} show a good linear relationship with the increase of Pr ion content. It can be seen from Fig. 4(g-h) that all elements except O_{ads} have a good linear relationship with the increase of Pr ion content, and O_{ads} has an inflection point at LSCFC-PH. This may be due to a large number of particle agglomerations on the surface of the cathode over-covering the ORR active sites of the internal LSCF, so the O_{ads} content began to decrease. In summary, the uniform multiphase core-shell structure formed by LSCF-PI in situ assembly can significantly

Table 2
The average valence of Co, Fe, and Pr ions in all cathodes.

Cathode	Co ion valence	Fe ion valence	Pr ion valence
LSCFC	2.48	3.07	-
LSCFC-PL	2.51	3.03	3.70
LSCFC-PI	2.55	2.99	3.68
LSCFC-PH	2.58	2.95	3.65

reduce the surface Sr content [9], and high concentrations of oxygen vacancies and mixed oxidation state Pr^{3+}/Pr^{4+} can improve the ORR activity and electronic conductivity of the cathode [40].

3.3. Electrical conductivity and thermogravimetry

Conductivity is one of the important factors to investigate the electrochemical performance of the cathode. Whether it is perovskite as a mixed ion-electronic conductor or spinel as a pure electronic conductor, the electronic conductivity inside the cathode is at least two orders of magnitude higher than the ionic conductivity, so the ionic conductivity can be ignored [41]. Fig. 5(a) shows the electrical conductivity of all cathodes. It can be seen that the electrical conductivity on both sides at ~350 °C shows an upward and downward trend, which is mainly caused by two reaction mechanisms. At low temperatures, the small polarons inside the cathode exhibit a thermally activated state, which is a typical semiconductor behavior [42,43]. However, when the temperature exceeds ~350 °C, the electrical conductivity shows a downward trend, showing the characteristics of a metal, which is related to the loss of O_{lat} at high temperatures and the release of oxygen vacancies through the reduction reaction of $Fe^{4+}(Fe^{3+})/Co^{3+}$ ions. The generation of oxygen vacancies blocks the path of charge transport, reduces the carrier concentration, and leads to a decline in electrical conductivity [44,45]. Furthermore, the cathode's electrical conductivity rises as the concentration of Pr ions increases, which is mainly because the Pr^{3+}/Pr^{4+} valence electron pair inside the cathode improves the ability of the cathode charge transport, so the electrical conductivity is improved [7, 42]. Fig. 5(b) shows the activation energy of electrical conductivity during all cathode thermal activations. The results show that the higher the content of Pr ions, the lower the energy barrier for small polaron hopping during thermal activation, and the higher the charge activity, which is advantageous for improving the electrocatalytic performance of the cathode. Fig. 5(c) shows the thermogravimetric (TG) curves of all the cathodes from room temperature to 800 °C. The weight loss phenomenon in the cathode at higher temperatures is caused by the oxygen vacancies released by O_{lat}, so observing the weight loss ratio of the cathode with temperature can directly observe the content of oxygen vacancies formed at high temperatures [46]. It can be seen from the TG curve that the increase of the content in Pr ions contributes to the generation of oxygen vacancies in the cathode at the operating temperature of the IT-SOFC. In addition, the conductivity is very sensitive to the change of oxygen partial pressure, which will cause the change of the cathode carrier and oxygen vacancy concentration, resulting in Electrical conductivity relaxation (ECR) phenomenon [47]. Figure S6 shows the ECR curve of LSCFC and LSCFC-PI sample strips when the oxygen partial pressure is 0.10 atm converted to 0.21 atm, and the chemical bulk diffusion coefficient (D_{chem}) and surface exchange coefficient (k_{chem}) are obtained by fitting. The K_{chem} (1.84 $cm^{-1}\times10^{-3}$) and D_{chem} (2.90 $cm^{-1}\times10^{-4}$) of LSCFC-PI formed by in situ assembly are much higher than those of LSCFC (K_{chem}=7.31 $cm^{-1}\times10^{-4}$; D_{chem}=9.63 $cm^{-1}\times10^{-5}$), indicating that LSCF-PI has better ORR kinetics.

3.4. Electrochemical impedance spectroscopy and CO_2 tolerance

To better analysis of cathode's ORR activity, we fabricated symmetrical cells with an electrode|GDC|electrode structure, and performed electrochemical impedance spectroscopy (EIS) tests in the temperature range of 550–700 °C. Among them, Fig. 6(a-c) and Figure S7 show the EIS spectra of LSCFC, LSCFC-PL, LSCFC-PI, and LSCFC-PH respectively. To facilitate comparison, we have deducted for the ohmic resistance resulting from the current collector and electrolyte thickness, and the data of ohmic resistance are in Table S2. It is evident from the EIS spectra that the presence of Pr ions leads to a notable decrease in the ASR value of the cathode, and the ASR of LSCFC-PI is the lowest, reaching 0.029 $\Omega\,cm^2$ at 700 °C, which means that the ORR activity of the cathode
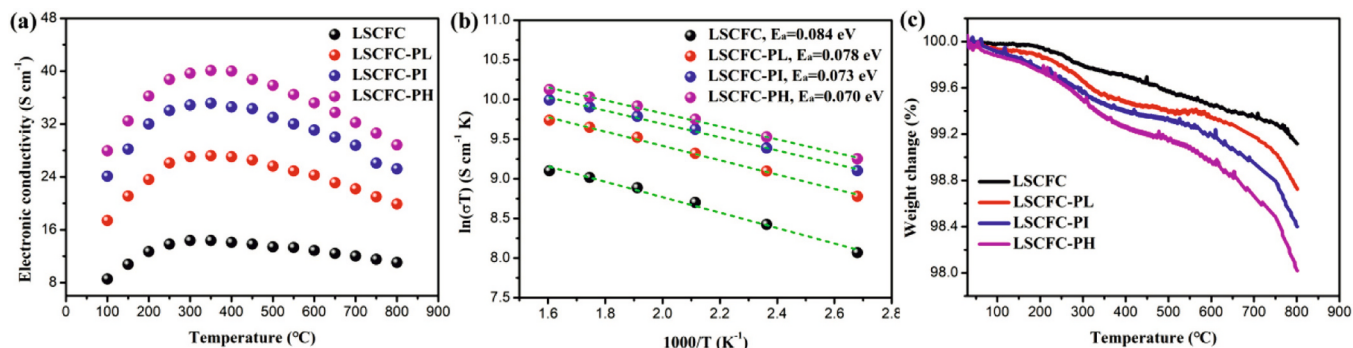
Fig. 5. (a) Electrical conductivity curves of all cathodes in the range of 100–800 °C, (b) Arrhenius plots of electrical conductivity, (c) TG curves of all cathodes in the temperature range from room temperature to 800 °C.

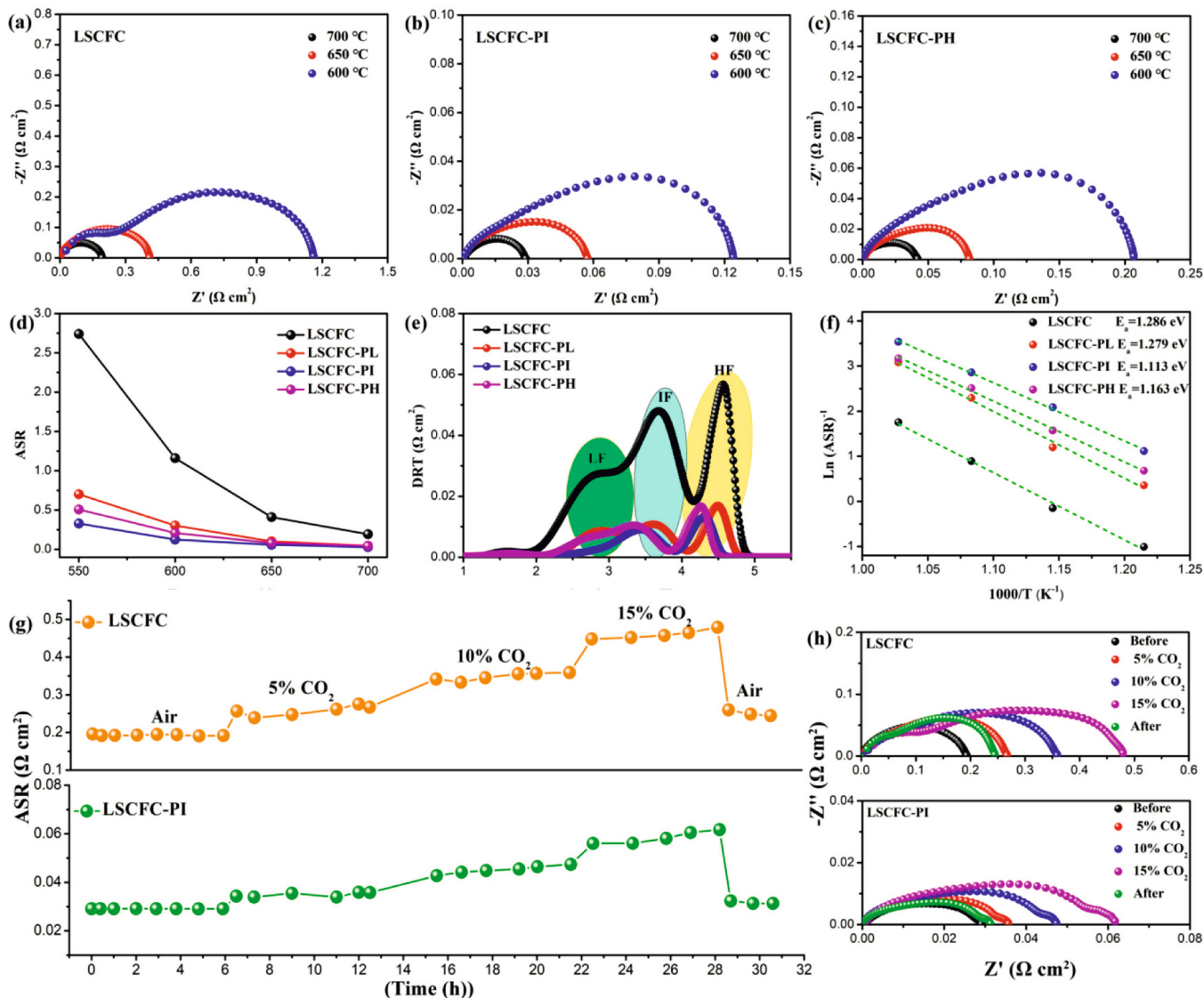**Fig. 6.** (a-c) EIS spectra of LSCFC, LSCFC-PI, LSCFC-PH at 600–800 °C, (d) ASR values for all symmetrical cells over the test temperature range, (e) DRT curves corresponding to the EIS of all cathodes at 700 °C, (f) Arrhenius curves corresponding to the ASR of all cathodes, (g) The CO$_2$ tolerance curves of LSCFC and LSCFC-PI and (h) the corresponding EIS spectra.

is the highest, which is lower than that of the original LSCFC (0.193 Ω cm^2) up ~6.7 times. This is mainly due to the in situ assembly of LSCFC-PI to form a uniform multiphase heterostructure, which promotes the ORR kinetics of the cathode [8,10]. However, ASR (0.042 Ω cm^2) of

LSCFC-PH begins to increase when Pr ions are excessive, which is mainly due to the obvious agglomeration phenomenon on the cathode surface caused by excessive Pr ions, which overcovers the ORR active site on the cathode surface and thus leads to the reduction of O$_{ads}$ on the surface [7,

28]. Therefore, the ORR activity of LSCFC-PH was decreased. Fig. 6(d) shows the summary curve of ASR for all cathodes within the test temperature. Table 3 summarizes the ASR values of different cathodes reported previously. It is evident that LSCFC-PI exhibits excellent electrocatalytic performance and holds great potential as a cathode for high-performance IT-SOFC. Figure S8 shows the EIS of LSCF and Pr composite cathodes with different A-site stoichiometry. It can be seen that the ASR values of several cathodes are higher than those of LSCFC-PI. This is mainly due to the uniform heterostructure of LSCFC-PI and the provision of more ORR active sites by surface nanoparticles, which promotes ORR kinetics. In addition, by comparing the EIS arcs of all cathodes, it can be seen that there are obvious differences between cathodes with different Pr ion contents, indicating a large change in the internal ORR kinetics. Fig. 6(e) shows the distribution of relaxation time (DRT) corresponding to EIS for all cathodes at 700 ℃. Usually, the characteristic peaks observed in DRT at various frequencies indicate diverse reaction mechanisms, and the integrated area of the peak is proportional to the resistance [48]. Among them, low frequency (LF), intermediate frequency (IF), and high frequency (HF) are related to surface gas diffusion, oxygen adsorption and dissociation, and charge transport processes, respectively [34,49]. It can be seen that the resistance of LSCFC in the three ORR reaction processes is relatively large compared with other cathodes. However, with the addition of Pr ions, the electrochemical performance of the cathode is greatly improved, especially the LF and IF parts decrease the most. Among them, the decrease in LF part is due to the uniform multiphase nanoparticles formed by in situ assembly providing more ORR active sites, increasing the specific surface area, and thus accelerating the surface gas diffusion rate [8]; The decrease of the IF part is due to the increasing of the concentration of oxygen vacancies inside the cathode, which accelerates the rate of oxygen adsorption and dissociation on the cathode surface [50]. In addition, HF may be related to the Pr^{3+}/Pr^{4+} valence electron pairs existing inside the cathode, which improves the conductivity of the cathode and thus increases the ability of charge transport. Fig. 6(f) compares the activation energy of ASR of all cathodes. The activation energy of LSCFC-PI (1.113 eV) is the lowest, indicating the lowest energy barrier of ORR, which is conducive to the occurrence of ORR [51].

Table 3
Summary of ASR for cathodes in different literatures.

Cathode	Electrolyte	ASR (Ω cm^2)	Reference
$La_{0.6}Sr_{0.4}Co_{0.2}Fe_{0.8}O_{3-\delta}$	GDC	0.158 (700 ℃)	[24]
$(La_{0.6}Sr_{0.4})_{0.95}Co_{0.2}Fe_{0.8}O_{3-\delta}$	GDC	0.123 (700 ℃)	[7]
$(La_{0.6}Sr_{0.4})_{0.95}Co_{0.2}Fe_{0.8}O_{3-\delta}$-$PrO_2$-$PrO2$		0.058 (700 ℃)	
$(La_{0.6}Sr_{0.4})_{0.90}Co_{0.8}Fe_{0.2}O_{3-\delta}$	GDC	0.050 (700℃)	[19]
$LaSr_{2.5}Co_{1.5}Fe_{1.5}O_{10-\delta}$	BZCY*	0.370 (600 ℃)	[53]
$(Mn_{0.6}Mg_{0.4})_{0.8}Sc_{0.2}Co_2O_4$-$PrO_{2-\delta}$	GDC	0.110 (750 ℃)	[37]
$La_{0.5}Ba_{0.5}CoO_{3-\delta}$	GDC	0.048 (700 ℃)	[29]
$La_{0.6}Sr_{0.4}Co_{0.2}Fe_{0.8}O_{3-\delta}$-GDC	GDC	0.093 (750℃)	[54]
$La_{0.5}Sr_{0.5}CoO_{3-\delta}$-$LaSrCoO_{4+\delta}$	SDC*	0.033 (800 ℃)	[55]
$La_{0.8}Sr_{0.2}FeO_{3-\delta}$- $La_{0.8}Sr_{1.2}FeO_{4-\delta}$	SDC*	0.156 (750 ℃)	[56]
LSCFC-PI	GDC	0.124 (600 ℃) 0.057 (650℃) 0.029 (700 ℃)	This Work

* BZCY: $BaZr_{0.1}Ce_{0.7}Y_{0.2}O_{3-\delta}$; SDC: $Sm_{0.2}Ce_{0.8}O_2$.

For SOFC cathodes, besides having a high ORR activity, it is equally important to consider the tolerance to noxious gases. Alkaline-earth metal cation Sr^{2+} is prone to produce carbonates under CO_2 atmosphere, which disrupts the stability of the structure [52]. Considering the greenhouse effect, it is necessary to investigate the tolerance of LSCFC and LSCFC-PI under CO_2 atmosphere. Fig. 6(g) shows the corresponding CO_2 tolerance test curve, and Fig. 6(h) shows the EIS spectra before and after the CO_2 tolerance test. When tested in the air for the first 6 h, the ASR of LSCFC and LSCFC-PI did not change. However, after the stability test under a CO_2 atmosphere, the ASR decay rates of LSCFC and LSCFC-PI were 21.0% and 6.5%, indicating that LSCFC-PI has better CO_2 tolerance.

To further confirm that CO_2-induced Sr segregation is the main factor leading to the decrease of ORR activity. Fig. 7(a-b) shows SEM and element mapping images of LSCFC and LSCFC-PI after the CO_2 tolerance test. It can be seen that Sr elements on the LSCFC surface are slightly agglomerated, while Sr elements on the LSCFC-PI surface are evenly distributed. In addition, it can be seen from the EDS images in Fig. 7(c-d) that the signal peak intensity of the Sr element in LSCFC is significantly higher than that of LSCFC-PI, and the signal peak intensity of the Co element in LSCFC-PI is higher than that of LSCFC. Fig. 8 shows a mechanism diagram of LSCFC and LSCFC-PI under a certain concentration of CO_2 atmosphere. As the surface Sr content of LSCFC is higher, the $SrCO_3$ insulating phase is formed under the action of the CO_2 atmosphere to cover the cathode surface, which reduces the contact area with O_2 in the air, and thus leads to the decrease of ORR activity [52]. Differently, in LSCFC-PI, Pr ion induced cathodic in situ assembly forms a uniform multiphase core-shell structure, which prevents the contact area between Sr and CO_2, provides a higher acidic environment, suppresses the segregation of Sr elements, and thus improves the tolerance to CO_2. Moreover, the $La_{0.6}Sr_{0.4}Co_xFe_yO_{3-\delta}/PrCoO_3/Co_3O_4/PrO_2$-type multiphase heterostructure formed inside LSCFC-PI not only promotes ORR kinetics [57], but also enhances the adhesion between electrodes and electrolytes interface by intertwined core-shell type nanostructure, thereby improving the stability and electrocatalytic activity of SOFC during operation [8,9]. Figure S9 and Figure S10 shows the FTIR and XRD patterns of LSCFC and LSCFC-PI powders calcined at 700 ℃ for 20 h in a 5% CO_2 atmosphere. There is no carbonate signal detected in the FT-IR pattern of LSCFC-PI, and there is no characteristic peak of $SrCO_3$ in the XRD pattern. Moreover, the XPS spectra of O 1 s and Sr 3d orbitals of the cathode after CO_2 atmosphere treatment are also shown in Figure S11 and Table S3. It can be seen that LSCFC-PI not only releases more oxygen vacancies from O_{lat} but also has a much lower $Sr_{surface}$ content than LSCFC. These results all indicate that LSCFC-PI has better CO_2 tolerance than LSCFC.

3.5. ORR dynamics and single cell performance

To better understand the cathode ORR kinetics, we performed EIS tests on the symmetrical cells operating at 700 ℃ while varying the oxygen partial pressures (P_{O2}). Fig. 9(a-b) shows the EIS spectra of LSCFC and LSCFC-PI at different P_{O2}, and Figure S12 is the corresponding DRT curve; Fig. 9(c) shows the dependence of ASR on P_{O2} in different reaction processes of LSCFC and LSCFC-PI. The relationship between ASR and P_{O2} is [42,58]:

$$ASR = ASR_0(P_{O2})^{-n} \tag{5}$$

Among them, ASR_0 is a constant, and n is related to the specific reaction process of ORR. The relationship between the rate-limiting step (RLS) and n is as follows[11,21,29]:

$$O_2 \Leftrightarrow O_{2,ads}, n = 1 \quad (\text{Oxygen adsorption process on the cathode surface}) \tag{6}$$

$$O_{2,ads} \Leftrightarrow 2O_{ads}, n = 0.5 \quad (\text{The dissociation process of adsorbed oxygen}) \tag{7}$$
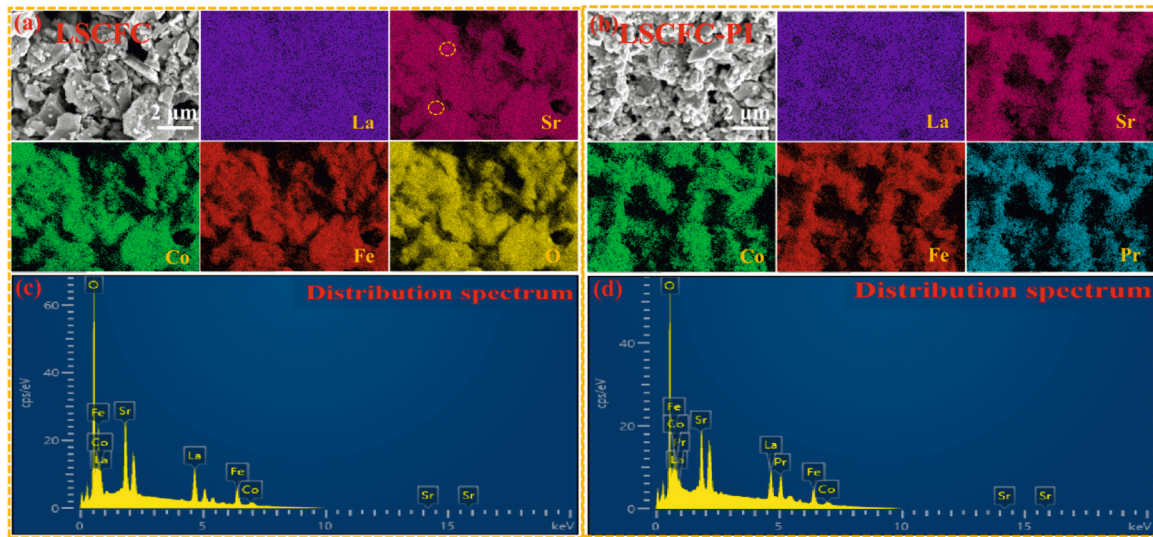
Fig. 7. (a-b) SEM and elemental mapping images and (c-d) corresponding EDS images of LSCFC and LSCFC-PI after CO_2 tolerance test.
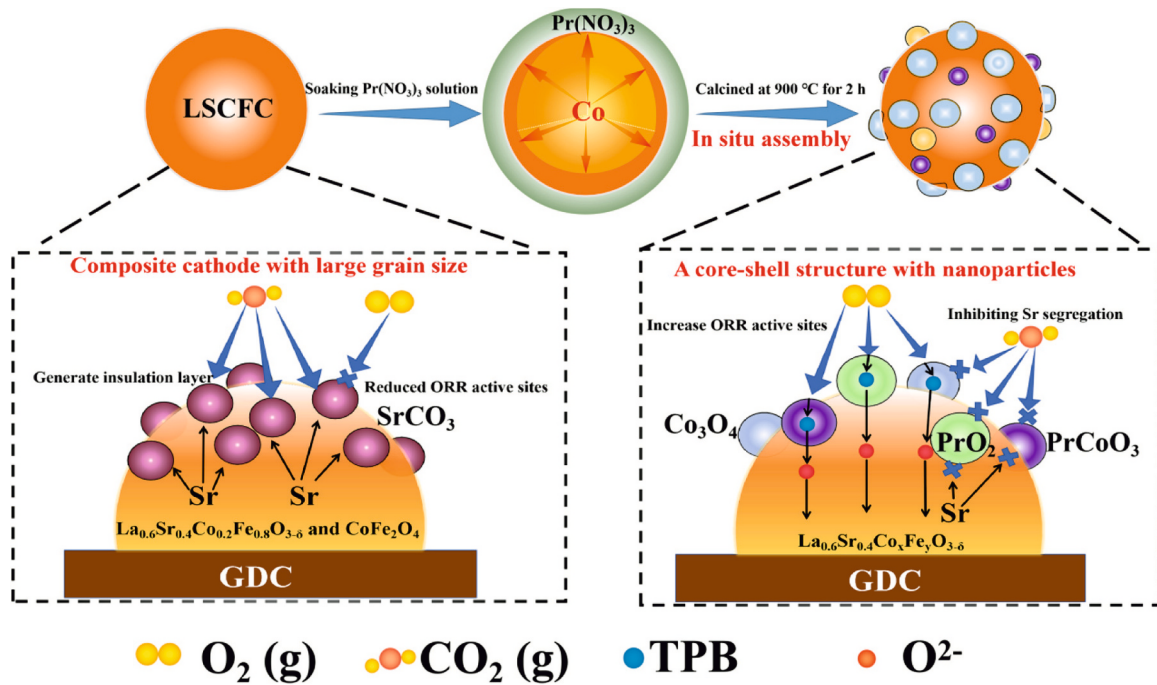

Fig. 8. ORR reaction mechanism of LSCFC and LSCFC-PI in a certain concentration of CO_2 atmosphere.

$$2O_{ads} + 2e^- + V_O^{\cdot\cdot} = O_O^\times, n = 0.25 \quad \text{(charge transport process)} \tag{8}$$

$$O_{electrode}^{2-} \Leftrightarrow O_{electrolyte}^{2-}, n = 0 \quad \text{(Oxygen ions are transported to the electrolyte through the TPB)} \tag{9}$$

It can be seen from RLS that the ORR kinetics of LSCFC and LSCFC-PI in the HF and IF regions are almost the same, and the dependence on P_{O2} is the lowest in the HF region ($n_{HF} = 0.09, 0.10$). It means that the RLS of the cathode in the HF region is mainly related to the transport of oxygen ions at the three-phase boundary (TPB). The n value of the cathode in the IF region is close to 0.25, so RLS is mainly a charge transport process. The RLS of LSCFC in the LF region is mainly due to the dissociation process of adsorbed oxygen ($n_{LF}=0.51$), and the difference is that the RLS of LSCFC-PI is due to the adsorption process of surface oxygen ($n_{LF}=0.83$). The difference in the LF region may be related to the

formation of the heterointerface that optimizes the internal structure of the cathode. Compared with LSCFC, LSCFC-PI promoted the dissociation process of adsorbed oxygen in the LF region, so the ORR kinetics in the LF region were significantly improved. In addition, the DRT curve of Figure S12 shows that the RLS of LSCFC is mainly IF and HF during the whole reaction process, while the RLS of LSCFC-PI is mainly HF. It is further confirmed that the multiphase heterostructure in LSCFC-PI optimizes the content of oxygen vacancy in the whole cathode, and the grain refinement increases the active site of ORR, thus accelerating the adsorption and dissociation rate of oxygen in the whole cathode. In addition, to further verify the ORR dynamic mechanism of the cathode, the equivalent circuit fitting of all EIS spectra was performed using ZView2 software (Inset of Fig. 9(a)), where capacitance (*C*) and angular relaxation frequency (*f*) as independent geometric parameters of the electrode can well elucidate the RLS. For the equivalent circuit, R1 is an
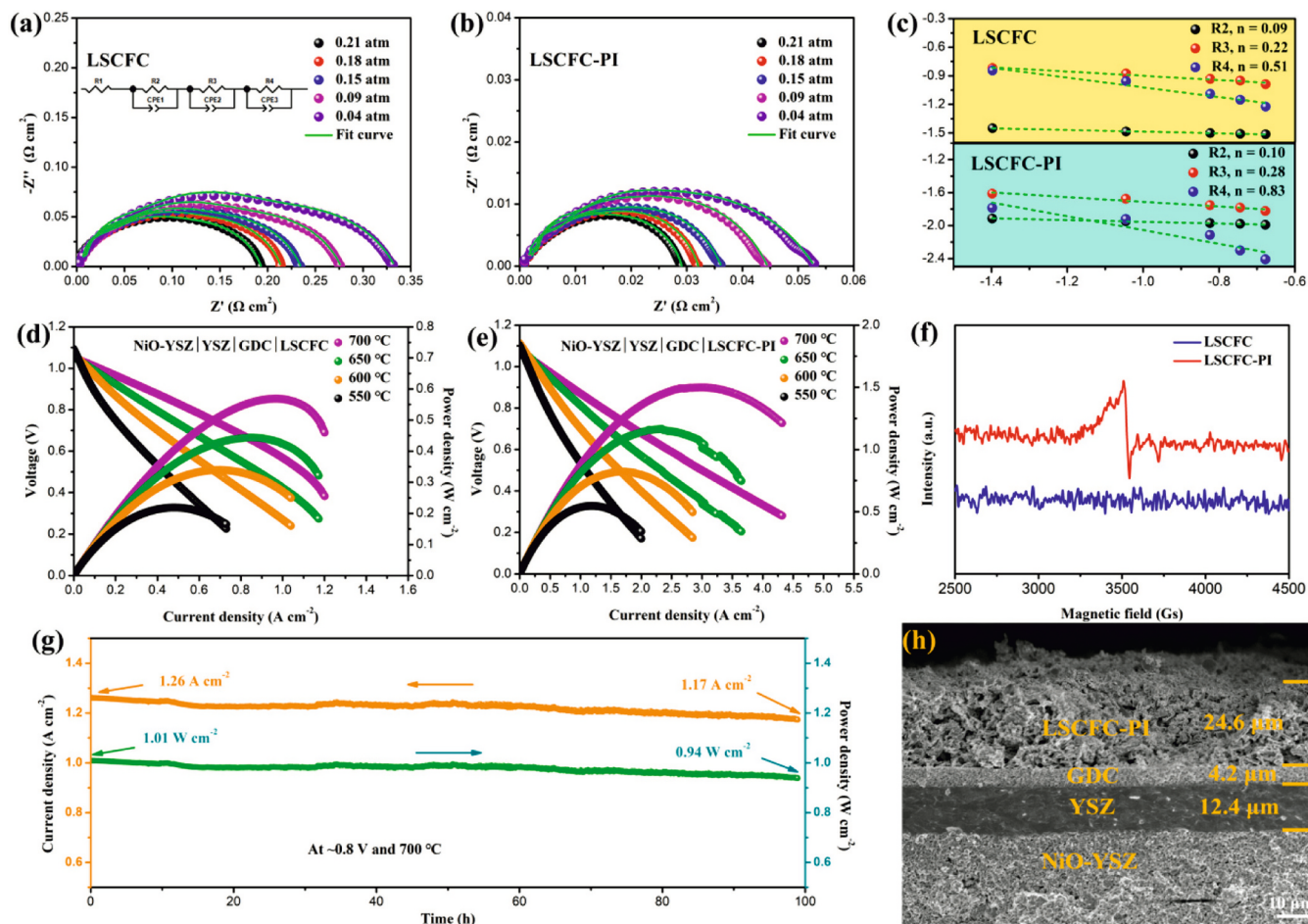
Fig. 9. (a-b) EIS spectra of LSCFC and LSCFC-PI at different P_{O_2} at 700 ℃ and (c) corresponding dependencies of R2, R3, and R4; (d-e) I-V-P curves of single cells prepared with LSCFC and LSCFC-PI as cathodes and EPR curves of corresponding powders; (g) Long-term stability test curve of the single cell with LSCFC-PI as the cathode at a constant voltage of ~0.8 V at 700 ℃ and (h) SEM image of the cross-section after the test.

ohmic resistance, R2, R3, and R4 represent the resistances of the three processes of HF, IF, and LF respectively, and CPE is related to the constant-phase element. Table S4 shows the corresponding fitting parameters. *C* and *f* can be calculated by the following formulas [11]:

$$Q_i = \sqrt[n_i]{CPE - T} \tag{10}$$

$$C_i = \frac{(R_i Q_i)^{1/n_i}}{R_i} \tag{11}$$

$$f_i = \frac{(R_i Q_i)^{-1/n_i}}{2\pi} \tag{12}$$

Among them, R_i is a resistance, Q_i is a constant phase element (non-ideal capacitor), n_i is similar to the actual capacitor, and CPE-P has the same meaning as n_i. Figure S14 shows *C* and *f* corresponding to LSCFC and LSCFC-PI. It can be seen that the values of *C* and *f* of LSCFC and LSCFC-PI in the HF region are close to the range of $\sim 10^{-6} \text{-} 10^{-7}$ F cm^{-2} and $\sim 10^7 \text{-} 10^8$ F cm^{-2}, respectively, which is consistent with the characteristics of oxygen ions passing through the electrode and electrolyte interface [34,59]. The *C* and *f* of the cathode in the IF region are in the range of $\sim 10^{-3} \text{-} 10^{-4}$ F cm^{-2} and $10^3 \text{-} 10^5$ F cm^{-2}, which is related to the charge transport after oxygen ion dissociation [60]. The *C* and *f* of LSCFC in the LF region are in the range of $\sim 10^{-1} \text{-} 10^{-2}$ F cm^{-2} and $1 \text{-} 10^2$ F cm^{-2}, indicating that the dissociation of adsorbed oxygen is RLS [11]. The difference is that the *C* and *f* of LSCFC-PI in the LF region are in the range of $\sim 1 \text{-} 10$ F cm^{-2} and $1 \text{-} 10^2$ F cm^{-2}, such a high capacitance does not belong to any ORR process, which is likely to be caused by the gas

diffusion process between the cathode gaps [45,61]. The results show that LSCFC-PI can optimize the whole ORR process compared with LSCFC. In addition, Figure S13 displays the bode plot representing the EIS spectra results of LSCFC and LSCFC-PI under varying PO_2 conditions, and the changing trend of the frequency is also in line with the P_{O_2} dependence. To better investigate the electrochemical performance of the cathode as an SOFC, we prepared a single cell with a cathode/GDC/YSZ/NiO structure supported by the anode. Fig. 9(d-e) shows the I-V-P curves of single cells with LSCFC and LSCFC-PI as the cathode. The open circuit voltage (OCV) of a single cell is close to Nernst's potential (~1.1 V) [62], indicating that it has good air tightness. At 700 ℃, the cathode with LSCFC-PI achieves a peak power density (PPD) of 1.51 W cm^{-2} for a single cell, which is approximately 2.65 times higher than that of LSCFC (0.57 W cm^{-2}). This is due to the improvement of the ORR activity and conductivity of the cathode by LSCFC-PI. In Table S5, we also compared the PPD of single cells that were prepared using various cathodes, which further showed that LSCFC-PI has excellent electrocatalytic performance. Fig. 9(f) shows that the oxygen vacancy of LSCFC and LSCFC-PI is tested by electron paramagnetic resonance (EPR) at room temperature. It can be seen that no oxygen vacancies were detected in LSCFC, but oxygen vacancies were formed in the uniformly multiphase LSCFC pi formed through in situ assembly modification. This is also the main factor that LSCFC-PI has excellent electrochemical performance. Fig. 9(g) shows the 100 h long-term stability test of a single cell with LSCFC-PI as the cathode at 700 ℃ and a constant voltage of ~0.8 V. After the long-term stability test, the decay rate of the current density of the single cell is only 0.09% h^{-1}, showing excellent long-term

stability. Fig. 9(h) shows the SEM image of the cross-section of the single cell after long-term stability testing. The single cell is composed of a porous structure cathode, GDC buffer layer, Y_2O_3 stabilized ZrO_2 (YSZ) electrolyte, and NiO-YSZ anode. In summary, LSCFC-PI not only has excellent ORR activity, but also has good long-term stability when used as a single-cell cathode, and is expected to become a promising IT-SOFC cathode.

4. Conclusions

XRD and TEM analysis showed that Pr-induced second phase decomposition of LSCFC, forming a uniform $La_{0.6}Sr_{0.4}Co_xFe_yO_{3-\delta}$/$PrCoO_3$/$Co_3O_4$/$PrO_2$ multiphase heterostructure through in situ assembly. Compared with LSCFC, LSCFC-PI not only improves the conductivity but also optimizes the content of internal oxygen vacancies, accelerates the oxygen adsorption and dissociation process, and improves the ORR kinetics. At 700 °C, the ASR value of LSCFC-PI reached 0.029 Ω cm^2, and the PPD when used as a single cell cathode reached 1.51 W cm^{-2}, which was greatly improved compared with 0.193 Ω cm^2 and 0.57 W cm^{-2} of LSCFC. The current density decay rate of the single cell with LSCFC-PI as the cathode is only 0.09% h^{-1} in the 100 h long-term stability test at 700 °C with a constant voltage of ~0.8 V, showing excellent long-term stability. In addition, the nanoparticles formed on the surface of LSCFC-PI not only inhibit the segregation of Sr elements and increase the acidity of the cathode surface, making LSCFC-PI have excellent CO_2 tolerance, but also the unique core-shell structure helps to enhance the adhesion between the cathode and electrolyte, improving the stability of the operation process. The in situ assembly of IT-SOFC cathodes with uniform multiphase heterostructures induced by rare earth ions is an effective strategy with development potential and innovation.

CRediT authorship contribution statement

Defeng Zhou: Writing – review & editing, Writing – original draft, Supervision, Resources. **Leilei Niu:** Investigation, Data curation. **Xiaofei Zhu:** Supervision, Resources, Investigation. **Ning Wang:** Supervision, Investigation, Resources, Software. **Qingwen Liang:** Software, Data curation. **Youjie Zhang:** Investigation, Data curation. **Ling Hu:** Investigation, Data curation. **Huifang Gong:** Investigation, Data curation. **Wenfu Yan:** Supervision, Resources. **Jinghe Bai:** Writing – original draft, Formal analysis, Data curation.

Declaration of Competing Interest

The authors declare that they have no known competing financial interests or personal relationships that could have appeared to influence the work reported in this paper.

Data availability

Data will be made available on request.

Appendix A. Supporting information

Supplementary data associated with this article can be found in the online version at doi:10.1016/j.apcatb.2024.124174.

References

[1] H. Chang, W. Tian, H. Chen, S.-D. Li, Z. Shao, Improved CO_2 electrolysis by a Fe nanoparticle-decorated (Ce, La, Sr)(CrFe)O$_{3-\delta}$ perovskite using a combined strategy of lattice defect-building, Electrochim. Acta 439 (2023) 141699, https://doi.org/10.1016/j.electacta.2022.141699.

[2] S. Pang, J. Xu, Y. Su, G. Yang, M. Zhu, M. Cui, X. Shen, C. Chen, The role of A-site cation size mismatch to tune the catalytic activity and durability of double perovskite oxides, Appl. Catal. B: Environ. 270 (2020), https://doi.org/10.1016/j.apcatb.2020.118868.

[3] H.A. Ishfaq, M.Z. Khan, M.T. Mehran, R. Raza, W.H. Tanveer, S. Bibi, A. Hussain, H.A. Muhammad, R.-H. Song, Boosting performance of the solid oxide fuel cell by facile nano-tailoring of La$_{0.6}$Sr$_{0.4}$CoO$_{3-\delta}$ cathode, Int. J. Hydrog. Energy 47 (2022) 37587–37598, https://doi.org/10.1016/j.ijhydene.2021.11.109.

[4] L. Wang, J. Li, X. Zhang, H. Sun, X. Guo, H. Zhang, W. Wang, Q. Hu, Synthesis and characterization of Bi$_{1-x}$Sr$_x$FeO$_{3-\delta}$(BSFO) nanofibers as cathodes for intermediate-temperature solid oxide fuel cells, Int. J. Hydrog. Energy 45 (2020) 27754–27763, https://doi.org/10.1016/j.ijhydene.2020.07.152.

[5] J. Gao, Q. Li, W. Xia, L. Sun, L.-H. Huo, H. Zhao, Advanced electrochemical performance and CO_2 tolerance of Bi$_{0.5}$Sr$_{0.5}$Fe$_{1-x}$Ti$_x$O$_{3-\delta}$ perovskite materials as oxygen reduction cathodes for intermediate-temperature solid oxide fuel cells, ACS Sustain. Chem. Eng. 7 (2019) 18647–18656, https://doi.org/10.1021/acssuschemeng.9b05086.

[6] J. Gao, Y. Liu, Y. Gao, M. Yuan, Z. Wang, Z. Lü, Q. Li, B. Wei, Cobalt-free fluorine doped Bi$_{0.7}$Sr$_{0.3}$FeO$_{3-\delta}$ oxides for energetic cathodes of low-temperature solid oxide fuel cells, Chem. Eng. J. 452 (2023) 139584, https://doi.org/10.1016/j.cej.2022.139584.

[7] H. Wang, W. Zhang, K. Guan, Z. Wei, J. Meng, J. Meng, X. Liu, Enhancing activity and durability of A-site-deficient (La$_{0.6}$Sr$_{0.4}$)$_{0.95}$Co$_{0.2}$Fe$_{0.8}$O$_{3-\delta}$ cathode by surface modification with PrO$_{2-\delta}$ nanoparticles, ACS Sustain. Chem. Eng. 8 (2020) 3367–3380, https://doi.org/10.1021/acssuschemeng.9b07354.

[8] Z. Chen, L. Jiang, S. He, C. Guan, Y. Zou, Z. Yue, N. Ai, S.P. Jiang, Y. Shao, K. Chen, Development of intertwined nanostructured multi-phase air electrodes for efficient and durable reversible solid oxide cells, Appl. Catal. B: Environ. 305 (2022) 121056, https://doi.org/10.1016/j.apcatb.2021.121056.

[9] Z. Yue, L. Jiang, Z. Chen, N. Ai, Y. Zou, S.P. Jiang, C. Guan, X. Wang, Y. Shao, H. Fang, Y. Luo, K. Chen, Ultrafine, dual-phase, cation-deficient PrBa$_{0.8}$Ca$_{0.2}$Co$_2$O$_{5+\delta}$ air electrode for efficient solid oxide cells, ACS Appl. Mater. Interfaces 15 (2023) 8138–8148, https://doi.org/10.1021/acsami.2c21172.

[10] K. Chen, N. Li, N. Ai, Y. Cheng, W.D.A. Rickard, S.P. Jiang, Polarization-Induced interface and Sr segregation of in situ assembled La$_{0.6}$Sr$_{0.4}$Co$_{0.2}$Fe$_{0.8}$O$_{3-\delta}$ electrodes on Y$_2$O$_3$–ZrO$_2$ electrolyte of solid oxide fuel cells, ACS Appl. Mater. Interfaces 8 (2016) 31729–31737, https://doi.org/10.1021/acsami.6b11665.

[11] F. Lu, T. Xia, Q. Li, J. Wang, L. Huo, H. Zhao, Heterostructured simple perovskite nanorod-decorated double perovskite cathode for solid oxide fuel cells: highly catalytic activity, stability and CO_2-durability for oxygen reduction reaction, Appl. Catal. B: Environ. 249 (2019) 19–31, https://doi.org/10.1016/j.apcatb.2019.02.056.

[12] C. Geng, H. Wu, Y. Yang, B. Wei, T. Hong, J. Cheng, A new in situ synthetic triple-conducting core–shell electrode for protonic ceramic fuel cells, ACS Sustain. Chem. Eng. 9 (2021) 11070–11079, https://doi.org/10.1021/acssuschemeng.1c02709.

[13] R. Zhou, Y. Gu, H. Dai, Y. Xu, L. Bi, In-situ exsolution of PrO$_{2-x}$ nanoparticles boost the performance of traditional Pr$_{0.5}$Sr$_{0.5}$MnO$_{3-\delta}$ cathode for proton-conducting solid oxide fuel cells, J. Eur. Ceram. Soc. 43 (2023) 6612–6621, https://doi.org/10.1016/j.jeurceramsoc.2023.06.054.

[14] H. Chen, Z. Guo, L.A. Zhang, Y. Li, F. Li, Y. Zhang, Y. Chen, X. Wang, B. Yu, J. M. Shi, J. Liu, C. Yang, S. Cheng, Y. Chen, M. Liu, Improving the electrocatalytic activity and durability of the La$_{0.6}$Sr$_{0.4}$Co$_{0.2}$Fe$_{0.8}$O$_{3-\delta}$ cathode by surface modification, ACS Appl. Mater. Interfaces 10 (2018) 39785–39793, https://doi.org/10.1021/acsami.8b14693.

[15] J. Bai, Z. Han, B. Lv, X. Chen, X. Zhu, D. Zhou, Preparation of 3D structure high performance Ba$_{0.5}$Sr$_{0.5}$Fe$_{0.8}$Cu$_{0.2}$O$_{3-\delta}$ nanofiber SOFC cathode material by low-temperature calcination method, Int. J. Hydrog. Energy 46 (2021) 8132–8142, https://doi.org/10.1016/j.ijhydene.2020.11.263.

[16] J. Zhou, P. Tang, J.-H. Bai, Y.-X. Chen, Y. Meng, X.-F. Zhu, N. Wang, D.-F. Zhou, W. Yan, A new type of Gd$_{0.2}$Ce$_{0.8}$O$_{3-\delta}$ fuel cell electrolyte containing Er$_{0.2}$Bi$_{0.8}$O$_{1.5}$ with highly improved performance, J. Alloy. Compd. 901 (2022) 163654, https://doi.org/10.1016/j.jallcom.2022.163654.

[17] S. Peng, Z. Yin, J. Xue, Tantalum doped La$_{0.6}$Sr$_{0.4}$FeO$_{3-\delta}$ electrodes for symmetrical proton conducting solid oxide fuel cells, React. Chem. Eng. 8 (2023) 737–944, https://doi.org/10.1039/D2RE00553K.

[18] O. Celikbilek, C.-A. Thieu, F. Agnese, E. Calì, C. Lenser, N.H. Menzler, J.-W. Son, S. J. Skinner, E. Djurado, Enhanced catalytic activity of nanostructured, A-site deficient (La$_{0.7}$Sr$_{0.3}$)$_{0.95}$(Co$_{0.2}$Fe$_{0.8}$)O$_{3-\delta}$ for SOFC cathodes, J. Mater. Chem. A 7 (2019) 25102–25111, https://doi.org/10.1039/c9ta07697b.

[19] J. Bai, D. Zhou, X. Zhu, N. Wang, R. Chen, B. Wang, W. Yan, In-situ segregation of A-site defect (La$_{0.6}$Sr$_{0.4}$)$_{0.90}$Co$_{0.2}$Fe$_{0.8}$O$_{3-\delta}$ to form a high-performance solid oxide fuel cell cathode material with heterostructure, Ceram. Int. 49 (2022) 5687–5699, https://doi.org/10.1016/j.ceramint.2022.10.295.

[20] C. Su, W. Wang, Z. Shao, Cation-deficient perovskites for clean energy conversion, Acc. Mater. Res. 2 (2021) 477–488, https://doi.org/10.1021/accountsmr.1c00036.

[21] J. Bai, D. Zhou, X. Zhu, N. Wang, R. Chen, B. Wang, New SOFC cathode: 3D core–shell-structured $La_{0.6}Sr_{0.4}Co_{0.2}Fe_{0.8}O_{3-\delta}@PrO_{2-\delta}$ nanofibers prepared by coaxial electrospinning, ACS Appl. Energy Mater. 5 (2022) 11178–11190, https://doi.org/10.1021/acsaem.2c01782.

[22] M. Yousaf, M. Akbar, M.A.K. Yousaf Shah, A. Noor, Y. Lu, M.N. Akhtar, N. Mushtaq, E. Hu, S. Yan, B. Zhu, Enhanced ORR catalytic activity of rare earth-doped Gd oxide ions in a $CoFe_2O_4$ cathode for low-temperature solid oxide fuel cells (LT-SOFCs), Ceram. Int. 48 (2022) 28142–28153, https://doi.org/10.1016/j.ceramint.2022.06.119.

[23] Y. Chen, C. Chen, D. Ding, Y. Ding, Y. Choi, L. Zhang, S. Yoo, D. Chen, B. deGlee, H. Xu, Q. Lu, B. Zhao, G. Vardar, J. Wang, H. Bluhm, E.J. Crumlin, C. Yang, J. Liu, B. Yildiz, M. Liu, A robust and active hybrid catalyst for facile oxygen reduction in solid oxide fuel cells, Energy Environ. Sci. 10 (2017) 964–971, https://doi.org/10.1039/c6ee03656b.

[24] W. Zhang, H. Wang, K. Guan, Z. Wei, X. Zhang, J. Meng, X. Liu, J. Meng, $La_{0.6}Sr_{0.4}Co_{0.2}Fe_{0.8}O_{3-\delta}/CeO_2$ heterostructured composite nanofibers as a highly active and robust cathode catalyst for solid oxide fuel cells, ACS Appl. Mater. Interfaces 11 (2019) 26830–26841, https://doi.org/10.1021/acsami.9b06668.

[25] J. Bai, Z. Han, D. Zhou, X. Zhu, N. Wang, R. Chen, J. He, W. Yan, Preparation of $Pr_2NiO_{4+\delta}-La_{0.6}Sr_{0.4}CoO_{3-\delta}$ as a high-performance cathode material for SOFC by an impregnation method, Int. J. Hydrog. Energy 48 (2023) 6076–6087, https://doi.org/10.1016/j.ijhydene.2022.11.123.

[26] A. Belotti, Y. Wang, A. Curcio, J. Liu, E. Quattrocchi, S. Pepe, F. Ciucci, The influence of A-site deficiency on the electrochemical properties of $(Ba_{0.95}La_{0.05})_{1-x}FeO_{3-\delta}$ as an intermediate temperature solid oxide fuel cell cathode, Int. J. Hydrog. Energy 47 (2022) 1229–1240, https://doi.org/10.1016/j.ijhydene.2021.10.098.

[27] M. Zhi, S. Lee, N. Miller, N.H. Menzler, N. Wu, An intermediate-temperature solid oxide fuel cell with electrospun nanofiber cathode, Energy Environ. Sci. 5 (2012) 7066, https://doi.org/10.1039/c2ee02619h.

[28] H. Wang, X. Zhang, W. Zhang, Z. Wei, K. Guan, J. Meng, F. Meng, J. Meng, X. Liu, Enhancing catalysis activity of $La_{0.6}Sr_{0.4}Co_{0.8}Fe_{0.2}O_{3-\delta}$ cathode for solid oxide fuel cell by a facile and efficient impregnation process, Int. J. Hydrog. Energy 44 (2019) 13757–13767, https://doi.org/10.1016/j.ijhydene.2019.03.184.

[29] L. Li, Z. Dong, T. Xia, X. Li, Q. Li, L. Sun, H. Zhao, L. Huo, A series of bifunctional $ReBaCo_2O_{5+\delta}$ perovskite catalysts towards intermediate-temperature oxygen reduction reaction and oxygen evolution reaction, Chem. Eng. J. 468 (2023) 143762, https://doi.org/10.1016/j.cej.2023.143762.

[30] J. Huang, Q. Liu, S.P. Jiang, L. Zhao, N. Ai, X. Wang, Y. Shao, C. Guan, H. Fang, Y. Luo, K. Chen, Promotional role of $BaCO_3$ on the chromium–tolerance of $La_{0.6}Sr_{0.4}Co_{0.2}Fe_{0.8}O_{3-\delta}$ cathodes of solid oxide fuel cells, Appl. Catal. B: Environ. 321 (2023), https://doi.org/10.1016/j.apcatb.2022.122080.

[31] W. Lee, J.W. Han, Y. Chen, Z. Cai, B. Yildiz, Cation size mismatch and charge interactions drive dopant segregation at the surfaces of manganite perovskites, J. Am. Chem. Soc. 135 (2013) 7909–7925, https://doi.org/10.1021/ja3125349.

[32] Y. Gou, G. Li, R. Ren, C. Xu, J. Qiao, W. Sun, K. Sun, Z. Wang, Pr-doping motivating the phase transformation of the $BaFeO_{3-\delta}$ perovskite as a high-performance solid oxide fuel cell cathode, ACS Appl. Mater. Interfaces (2021) 20174–20184, https://doi.org/10.1021/acsami.1c03514.

[33] N.C. Jeong, J.S. Lee, E.L. Tae, Y.J. Lee, K.B. Yoon, Acidity scale for metal oxides and Sanderson's electronegativities of lanthanide elements, Angew. Chem. Int. Ed. 47 (2008) 10128–10132, https://doi.org/10.1002/anie.200803837.

[34] J. Bai, D. Zhou, X. Zhu, N. Wang, Q. Liang, R. Chen, H. Lu, J. Li, W. Yan, $Bi_{0.5}Sr_{0.5}FeO_{3-\delta}$ perovskite B-site doped Ln (Nd, Sm) as cathode for high performance Co-free intermediate temperature solid oxide fuel cell, Ceram. Int. 49 (2023) 28682–28692, https://doi.org/10.1016/j.ceramint.2023.06.124.

[35] L. Gao, Q. Li, L. Sun, T. Xia, L. Huo, H. Zhao, J.-C. Grenier, Antimony-doped $Bi_{0.5}Sr_{0.5}FeO_{3-\delta}$ as a novel Fe-based oxygen reduction electrocatalyst for solid oxide fuel cells below 600 °C, J. Mater. Chem. A 6 (2018) 15221–15229, https://doi.org/10.1039/c8ta04222e.

[36] S. Zhang, Y. Wan, Z. Xu, S. Xue, L. Zhang, B. Zhang, C. Xia, Bismuth doped $La_{0.75}Sr_{0.25}Cr_{0.5}Mn_{0.5}O_{3-\delta}$ perovskite as a novel redox-stable efficient anode for solid oxide fuel cells, J. Mater. Chem. A 8 (2020) 11553–11563, https://doi.org/10.1039/d0ta03328f.

[37] H. Wang, W. Zhang, J. Meng, Y. Pei, X. Qiu, F. Meng, X. Liu, Effectively promoting activity and stability of a $MnCo_2O_4$-based cathode by in situ constructed heterointerfaces for solid oxide fuel cells, ACS Appl. Mater. Interfaces 13 (2021) 24329–24340, https://doi.org/10.1021/acsami.1c06757.

[38] J. Meng, N. Xu, X. Wang, F. Yao, C. Tian, X. Liu, L. Zhao, Z. Xu, Highly efficient and stable intermediate-temperature solid oxide fuel cells using Bi-deficient perovskite cathode, Int. J. Hydrog. Energy 48 (2023) 33620–33632, https://doi.org/10.1016/j.ijhydene.2023.05.111.

[39] Q. Ji, L. Bi, J. Zhang, H. Cao, X.S. Zhao, The role of oxygen vacancies of ABO_3 perovskite oxides in the oxygen reduction reaction, Energy Environ. Sci. 13 (2020) 1408–1428, https://doi.org/10.1039/d0ee00092b.

[40] S. Lei, A. Wang, G. Weng, Y. Wu, J. Xue, H. Wang, Simultaneous generation of electricity, ethylene and decomposition of nitrous oxide via protonic ceramic fuel cell membrane reactor, J. Energy Chem. 77 (2023) 359–368, https://doi.org/10.1016/j.jechem.2022.10.035.

[41] S. Wang, F. Jin, L. Li, R. Li, B. Qu, T. He, Stability, compatibility and performance improvement of $SrCo_{0.8}Fe_{0.1}Nb_{0.1}O_{3-\delta}$ perovskite as a cathode for intermediate-temperature solid oxide fuel cells, Int. J. Hydrog. Energy 42 (2017) 4465–4477, https://doi.org/10.1016/j.ijhydene.2016.11.015.

[42] W. Zhang, L. Zhang, K. Guan, X. Zhang, J. Meng, H. Wang, X. Liu, J. Meng, Effective promotion of oxygen reduction activity by rare earth doping in simple perovskite cathodes for intermediate-temperature solid oxide fuel cells, J. Power Sources 446 (2020) 227360, https://doi.org/10.1016/j.jpowsour.2019.227360.

[43] C. Yao, J. Yang, H. Zhang, X. Lang, K. Cai, Ca-doped $PrBa_{1-x}Ca_xCoCuO_{5+\delta}$ (x = 0–0.2) as cathode materials for solid oxide fuel cells, Ceram. Int. 48 (2022) 7652–7662, https://doi.org/10.1016/j.ceramint.2021.11.310.

[44] B. Zhang, Y. Wan, Z. Hua, K. Tang, C. Xia, Tungsten-doped $PrBaFe_2O_{5+\delta}$ double perovskite as a high-performance electrode material for symmetrical solid oxide fuel cells, ACS Appl. Energy Mater. 4 (2021) 8404–8409, https://doi.org/10.1021/acsaem.1c01618.

[45] L. Zhang, S. Li, T. Xia, L. Sun, L. Huo, H. Zhao, Co-deficient $PrBaCo_{2-x}O_{6-\delta}$ perovskites as cathode materials for intermediate-temperature solid oxide fuel cells: enhanced electrochemical performance and oxygen reduction kinetics, Int. J. Hydrog. Energy 43 (2018) 3761–3775, https://doi.org/10.1016/j.ijhydene.2018.01.018.

[46] W. Zhang, J. Meng, X. Zhang, L. Zhang, X. Liu, J. Meng, Co-incorporating enhancement on oxygen vacancy formation energy and electrochemical property of $Sr_2Co_{1+x}Mo_{1-x}O_{6-\delta}$ cathode for intermediate-temperature solid oxide fuel cell, Solid State Ion. 316 (2018) 20–28, https://doi.org/10.1016/j.ssi.2017.12.015.

[47] C.C. Wang, T. Becker, K. Chen, L. Zhao, B. Wei, S.P. Jiang, Effect of temperature on the chromium deposition and poisoning of $La_{0.6}Sr_{0.4}Co_{0.2}Fe_{0.8}O_{3-\delta}$ cathodes of solid oxide fuel cells, Electrochim. Acta 139 (2014) 173–179, https://doi.org/10.1016/j.electacta.2014.07.028.

[48] Y. Kong, C. Sun, X. Wu, K. Sun, X. Yin, N. Zhang, One-dimensional $CuCo_2O_4–Er_{0.4}Bi_{1.6}O_3$ composite fiber as cathode of intermediate temperature solid oxide fuel cells, ACS Sustain. Chem. Eng. 8 (2020) 3950–3958, https://doi.org/10.1021/acssuschemeng.9b07727.

[49] J. Liu, F. Ciucci, The Gaussian process distribution of relaxation times: a machine learning tool for the analysis and prediction of electrochemical impedance spectroscopy data, Electrochim. Acta 331 (2020) 135316, https://doi.org/10.1016/j.electacta.2019.135316.

[50] S. Zhai, S. Xie, P. Cui, D. Guan, J. Wang, S. Zhao, B. Chen, Y. Song, Z. Shao, M. Ni, A combined ionic Lewis acid descriptor and machine-learning approach to prediction of efficient oxygen reduction electrodes for ceramic fuel cells, Nat. Energy 7 (2022) 866–875, https://doi.org/10.1038/s41560-022-01098-3.

[51] W. Zhang, H. Wang, X. Chen, X. Liu, J. Meng, Manipulation of rare earth on voltage-driven in-situ exsolution process of perovskite cathodes for low-temperature solid oxide fuel cells, Chem. Eng. J. 446 (2022) 136934, https://doi.org/10.1016/j.cej.2022.136934.

[52] G. Weng, S. Lei, R. Wang, K. Ouyang, J. Dong, X. Lin, J. Xue, L.-X. Ding, H. Wang, A high-efficiency electrochemical proton-conducting membrane reactor for ammonia production at intermediate temperatures, Joule 7 (2023) 1333–1346, https://doi.org/10.1016/j.joule.2023.05.013.

[53] H. Shi, C. Su, X. Xu, Y. Pan, G. Yang, R. Ran, Z. Shao, Building Ruddlesden-Popper and single perovskite nanocomposites: a new strategy to develop high-performance cathode for protonic ceramic fuel cells, Small 17 (2021) 2101872, https://doi.org/10.1002/smll.202101872.

[54] Z. Zheng, J. Jing, H. Yu, Z. Yang, C. Jin, F. Chen, S. Peng, Boosting and robust multifunction cathode layer for solid oxide fuel cells, ACS Sustain. Chem. Eng. 10 (2022) 6817–6825, https://doi.org/10.1021/acssuschemeng.2c01383.

[55] F. Li, L. Jiang, R. Zeng, F. Wang, Y. Xu, Y. Huang, Hetero-structured $La_{0.5}Sr_{0.5}CoO_{3-\delta}/LaSrCoO_{4+\delta}$ cathode with high electro-catalytic activity for solid-oxide fuel cells, Int. J. Hydrog. Energy 42 (2017) 29463–29471, https://doi.org/10.1016/j.ijhydene.2017.10.001.

[56] T. Hong, M. Zhao, K. Brinkman, F. Chen, C. Xia, Enhanced oxygen reduction activity on ruddlesden-popper phase decorated $La_{0.8}Sr_{0.2}FeO_{3-\delta}$ 3D heterostructured cathode for solid oxide fuel cells, ACS Appl. Mater. Interfaces 9 (2017) 8659–8668, https://doi.org/10.1021/acsami.6b14625.

[57] C. Yan, C. Zhuhua, K. Yener, M. Wen, T.H. L, Y. Bilge, Electronic activation of cathode superlattices at elevated temperatures – source of markedly accelerated oxygen reduction kinetics, Adv. Energy Mater. 3 (2013) 1221–1229, https://doi.org/10.1002/aenm.201300025.

[58] J. Gao, Y. Liu, T. Xia, L. Sun, H. Zhao, B. Wei, Q. Li, Advanced electrochemical activity and CO_2 tolerance of iron-based cathode electrocatalyst for solid oxide fuel cells, Sep. Purif. Technol. 311 (2023) 123267, https://doi.org/10.1016/j.seppur.2023.123267.

[59] J.S.A. Carneiro, R.A. Brocca, M.L.R.S. Lucena, E. Nikolla, Optimizing cathode materials for intermediate-temperature solid oxide fuel cells (SOFCs): oxygen reduction on nanostructured lanthanum nickelate oxides, Appl. Catal. B: Environ. 200 (2017) 106–113, https://doi.org/10.1016/j.apcatb.2016.06.073.

[60] M.J. Escudero, A. Aguadero, J.A. Alonso, L. Daza, A kinetic study of oxygen reduction reaction on La_2NiO_4 cathodes by means of impedance spectroscopy, J. Electroanal. Chem. 611 (2007) 107–116, https://doi.org/10.1016/j.jelechem.2007.08.006.

[61] X. Li, X. Jiang, S.Shengli Pang, S. Wang, Z. Su, Q. Zhang, Effect of iron substitution content on structure, thermal expansion behavior and electrochemical properties of $La_{0.5}Ba_{0.5}Co_{1-y}Fe_yO_{3-\delta}$, Int. J. Hydrog. Energy 36 (2011) 13850–13857, https://doi.org/10.1016/j.ijhydene.2011.07.083.

[62] J. Wang, X. Chen, S. Xie, L. Chen, Y. Wang, J. Meng, D. Zhou, Bismuth tungstate/neodymium-doped ceria composite electrolyte for intermediate-temperature solid oxide fuel cell: sintering aid and composite effect, J. Power Sources 428 (2019) 105–114, https://doi.org/10.1016/j.jpowsour.2019.04.105.